

# Mesospheric temperature during the extreme mid-latitude noctilucent cloud event on 18/19 July 2016

N. Kaifler<sup>1</sup>, B. Kaifler<sup>1</sup>, H. Wilms<sup>1</sup>, M. Rapp<sup>1</sup>, G. Stober<sup>2</sup>, C. Jacobi<sup>3</sup>

---

N. Kaifler, natalie.kaifler@dlr.de

<sup>1</sup>Institut für Physik der Atmosphäre,

Deutsches Zentrum für Luft- und

Raumfahrt, Oberpfaffenhofen, Germany

<sup>2</sup>Leibniz-Institute of Atmospheric Physics,

Kühlungsborn, Germany

<sup>3</sup>University of Leipzig, Institute for

Meteorology, Leipzig, Germany

This article has been accepted for publication and undergone full peer review but has not been through the copyediting, typesetting, pagination and proofreading process, which may lead to differences between this version and the Version of Record. Please cite this article as doi: 10.1029/2018JD029717

**Abstract.** A rare noctilucent cloud (NLC) event was observed at 48.8°N, 13.7°E above GERES station in southern Germany on 18/19 July 2016 using the CORAL Rayleigh lidar. Strong southward winds due to a quasi 2-day planetary wave allowed for the influx of mesospheric polar air to mid-latitudes on this day. The NLC observed by lidar was preceded by strong NLC displays in CIPS satellite images above the North Sea and by strong MSE radar echoes 800 km north of the lidar site, and was also observed visually in central Europe. The NLC occurred at low altitude and was bright and thin with strong oscillations in altitude and brightness. Darkness allowed for high-resolution temperature measurements at NLC altitudes. The ice particles were embedded in the upper part of a cold region with temperatures below 150 K. Significantly higher temperatures were found directly above the cloud with large vertical temperature gradients of 25 K/km at the top boundary. Spectral analysis reveals that NLC particles existed within cold phases of gravity waves within a region of high static stability. In order to study the evolution of NLC brightness in this environment we drive the microphysical model CARMA with lidar temperature soundings. We find that NLC particles can survive and grow in the conditions defining this mid-latitude event. We conclude that the ice particles did not nucleate at the site of observation, but were meridionally transported and vertically confined to a thin layer due to a large vertical temperature gradient, wind reversal, and low levels of mesospheric turbulence.

**Keypoints:**

- A bright noctilucent cloud is advected from northern to mid-latitudes

during a strong 2-day planetary wave event

- A large vertical temperature gradient, wind reversal, and low levels of turbulence confine NLC to a thin layer
- Ice particles reside and grow within the cold phases of gravity waves

## 1. Introduction

Noctilucent clouds (NLC) consist of ice particles forming in the polar mesopause region during summer, when extremely low temperatures of 150 K and below are reached [*Theon et al.*, 1967; *Thomas*, 1991; *Rapp and Lübken*, 2004, their Fig. 1]. The ice particles nucleate on meteoric smoke particles around the mesopause and subsequently sediment to lower altitudes while growing [*Rapp and Thomas*, 2006]. Rapid sublimation then occurs at the lower boundary when the background temperature increases. *Kiliani et al.* [2013] determined the total lifetime of the ice particles to be  $36 \pm 24$ h, during which time the particles are subject to zonal transport by mesospheric winds. NLC form during supersaturated conditions, and their occurrence is critically dependent on temperature and the availability of water vapor [e.g. *Rapp and Thomas*, 2006; *Rong et al.*, 2012].

The exact relation between NLC properties and atmospheric temperature, however, is difficult to determine, making temperature measurements within NLC highly valuable.

The first report of combined NLC and temperature soundings using the lidar technique is by *von Cossart et al.* [1996] who showed two one hour-integrated temperature profiles shortly before a NLC detection at 54°N. *Gerding et al.* [2007a] and *Gerding et al.* [2007b] presented three NLC measurements of 1 h, 45 min and 2.5 h duration within a 3 or 4 km vertical temperature gap in temperature measurements, also obtained at 54°N. *Chu et al.* [2011] report three NLC detections of less than 1 h duration at McMurdo, Antarctica (78°S) and temperatures obtained by iron resonance sounding above the NLC layer. Combinations of two instruments were also used to study NLC. *Lübken et al.* [1996, 2004] performed in-situ temperature measurements at NLC altitudes during rocket

launches from Andøya (69°N) and Spitsbergen (78°N). Coincident lidar measurements show NLC at the lower boundary of the cold region, approximately 6 km below the temperature minimum. *Rapp et al.* [2002] reported combined lidar observations of NLC and sounding rocket measurements of temperatures and found that the NLC were located in a temperature minimum due to inertia gravity waves. Simultaneous and common-volume temperature soundings are obtained from the SOFIE instrument aboard the AIM satellite [*Hervig et al.*, 2009]. By means of a tomographic retrieval, temperature within the NLC layer is also obtained from the Sub-Millimeter Radiometer (SMR) and Optical Spectrograph and InfraRed Imaging System (Osiris) instruments aboard the Odin satellite [*Christensen et al.*, 2015, 2016]. The vertical resolution of the retrieved temperature data is 2.5 km. Their Fig. 14 and Fig. 5, respectively shows that NLC backscatter follows the temperature isolines in an observation north of 70°N.

In principle the lidar technique is ideally suited for middle-atmosphere soundings, as it allows for routine, high-resolution measurements in the entire altitude range. Although lidars are in theory capable of measuring both temperature and NLC backscatter, the presence of NLC particles inherently prevents temperature measurements within the NLC layer for the following reasons: (1) the strong Mie scatter from the ice particles contaminates the Rayleigh signal used for hydrostatic integration, and (2) the scattering off the metal atoms in the metal layer utilized by resonance lidars is reduced by ice coating during the presence of NLC [*Plane et al.*, 2004]. Because of these facts, previous studies were restricted to a combination of Rayleigh temperatures below the NLC layer and temperatures obtained from metal lidars above the NLC layer, with significant vertical gaps in the temperature profiles where the NLC layer resides. So far, no Rayleigh lidar at polar lati-

tudes is powerful enough to reach top altitudes above the NLC layer given the high solar background. It is therefore advantageous to detect NLC during darkness. However, NLC are most abundant at high latitudes and rarest at mid latitudes [e.g. *Hervig et al.*, 2009].

The decrease in NLC occurrence with decreasing latitude arises due to higher mesospheric temperature and therefore reduced ice mass density, e.g. shown by comparisons of NLC lidar soundings with SOFIE satellite measurements [*Hervig et al.*, 2016].

The question whether the occurrence of mid-latitude NLC increased during the last two decades is heavily debated, and is closely tied to the question of their origin. *Nielsen et al.* [2011] state that NLC occurrence at mid-latitude is due to a combination of advection from higher latitudes and growth during times of enhanced 5-day planetary wave activity. *Gerding et al.* [2007b] also rate advection and favourable conditions during the growth of the particles above local conditions at the observation site. *Suzuki et al.* [2016] attribute a NLC observed in 2015 by cameras from 44°N to southward advection unrelated to local mesospheric temperature anomalies. *Russell et al.* [2014] on the other hand argue that a trend towards lower mesospheric temperatures is responsible for the increased number of observations of mid-latitude NLC based on modelled NLC occurrences using satellite data. *Hultgren et al.* [2011] argue for local formation in an unusually cold mesosphere in connection with favourable phases of the diurnal tide and of planetary waves in a 2009 NLC case at mid-latitudes.

The lowest latitude for NLC observations, 42°N, was reported by *Wickwar et al.* [2002] by visual sighting and lidar measurements. In Europe, a network of automatic NLC cameras detected the southernmost NLC above 42.7°N, observed from 37.2°N [*Russell et al.*, 2014]. *Russell et al.* [2014] also show NLC occurrence rates of 10–20 % in the 40–

60°N latitude band obtained from OSIRIS. At 54°N, typically 2–3 NLC events totaling 4 h are observed by lidar each summer [Gerding *et al.*, 2013]. Visual observations in the southern hemisphere, mostly from Tierra del Fuego, are rare [Fogle, 1966]. It is worth mentioning that the instrument utilized in the study at hand observed NLC during two nights in the 2017/2018 season at Rio Grande, Tierra del Fuego, Argentina at 53.78°S. These events will be described elsewhere.

In this work, we present high-resolution Rayleigh lidar temperature measurements in direct vicinity of a NLC utilizing a rare NLC observation at a northern-hemisphere mid-latitude site at 48.8°N. The high signal-to-noise ratio achieved by the operation of a high-power lidar in darkness and a low, thin-layered NLC enabled us to push the temperature retrieval to altitudes above the NLC layer and refine it in order to derive temperatures within the NLC layer by interpolation.

Instrument, dataset and the extended temperature retrieval are described in section 2. Section 3 shows the NLC observation on 18/19 July 2016 and accompanying temperature soundings. The analysis of local dynamics in section 4 includes an assessment of the motions of the NLC layer as well as gravity wave structures derived from temperature perturbations. The interplay between the growth of NLC particles and the local background is further explored using simulations with the microphysical model CARMA. Section 5 provides additional evidence for horizontal transport of NLC particles including mesospheric wind measurements, satellite and radar observations in the extended area. In section 6, we relate the observed single event to statistics of mid-latitude NLC including the occurrence rate and the thermal structure.

## 2. Instrument and data processing

### 2.1. Rayleigh lidar

The Compact Rayleigh Autonomous Lidar (CORAL) conducted middle atmospheric soundings at the GERman Experimental Seismic System (GERES) station atop Sulzberg (1140 m, 48.84°N, 13.70°E) in the Bavarian Forest, Germany, in 2016. The autonomous Rayleigh lidar employed a pulsed Nd:YAG laser of 12 W output power at 532 nm wavelength and detected the atmospheric return signal using a telescope of 63 cm diameter and two height-cascaded receiving channels. Results from previous campaigns of this instrument regarding the observation of secondary gravity waves were published by *Kaifler et al.* [2017]. Between 2 May and 28 November 2016, nearly 500 h of scientific data were acquired at GERES station. In June and July, operations were possible between 21 and 2 UT when the sun was at least 7° below the horizon.

The NLC brightness is determined by conversion of the backscatter ratio to volume backscatter coefficient  $\beta$  by normalization to the MSIS-E-90 density profile between 42 and 78 km altitude [Thayer et al., 1995; Fiedler et al., 2011]. Time series of NLC parameters such as centroid altitude ( $z_c$ ), top and bottom boundary of the layer determined by the instrument sensitivity of  $\beta = 0.1 \times 10^{-10} \text{m}^{-1} \text{sr}^{-1}$ , as well as maximum and integrated brightness ( $\beta_{\text{max}}, \beta_{\text{int}}$ ) of the layer are derived with a temporal resolution of 2 min.

In the absence of NLC particles, temperature is found by a multi-step integration method of density profiles with 90 m vertical resolution and different temporal resolutions. In a first step the nightly mean density profile is hydrostatically integrated following *Hauchecorne and Chanin* [1980] with an initial value taken from the closest SABER temperature measurement at 100 km altitude with less than 300 km horizontal distance



[Russell III *et al.*, 1994]. Then, the analysis is repeated for the next higher temporal resolution using temperatures of the previously retrieved profiles as seed values. This way, temperature datasets are constructed with temporal resolutions of the duration of the night, 120 min, 60 min, 30 min, 20 min, and 15 min in the altitude range 30–96 km, with the top altitude depending on temporal resolution. Profiles are vertically smoothed with a window of 630 m length.

## 2.2. Temperature retrieval from NLC-perturbed density profiles

No vertically resolved temperature measurement within the NLC layer can be obtained using Rayleigh lidar, as it is impossible to separate the Rayleigh signal from the much stronger Mie peak. It is however possible to obtain a mean temperature by means of interpolation of the molecular backscatter profile through the NLC layer (e.g. *Gerding et al.* [2007a]). The temperature integration can then be performed as usual, which works particularly well for thin NLC layers.

To determine the NLC layer boundary, we fit two exponential functions, one within a range of 3 km above and one within a range of 2 km below the layer (purple and blue lines in Fig.1a). Each altitude ranges is shifted towards the NLC layer until the value of  $\chi^2$  increases significantly, indicating the presence of NLC backscatter. Measurements within the so found NLC layer are removed. An exponential function is then fitted over both ranges above and below the layer (yellow line in Fig.1a) to estimate density within the NLC layer (assuming pure Rayleigh scattering, photon counts are proportional to atmospheric density). The example at 1 UT on 19 July in Fig.1 clearly shows a jump in atmospheric density occurring between the two fit ranges. This indicates lower temperatures within the NLC layer as compared to above and below. Because the fit is more

tightly constrained in the range below the layer due to better photon count statistics, we estimate the temperature error within the NLC layer caused by the interpolation to be asymmetrical with about +2 K and -10 K. Due to top-down integration with 630 m effective resolution, the temperature down to 315 m above the NLC layer is unaffected by the interpolation. We apply this technique to photon count profiles integrated over 60 s (6000 laser pulses). Poisson noise is then added to the interpolated part of the profile. Finally, the so modified profiles with the NLC removed are integrated over intervals of 15 min, shifted successively by 60 s, and mean temperature profiles are found from an ensemble of 100 retrieval runs per profile.

### 3. Observations

#### 3.1. NLC detection and characteristics

The only NLC observation in the 2016 season at GERES station was recorded by the CORAL lidar on the night of 18/19 July 2016 (day of year 199 or 28 days from solstice) for a duration of 4.9 hours. Backscatter from NLC particles was detected between 19:51–20:47 UT and between 21:55–1:49 UT. The highest backscatter ratio of 49.4 was detected at 1:07 UT, and corresponds to a maximum NLC brightness of  $\beta = 11.7 \times 10^{-10} \text{m}^{-1} \text{sr}^{-1}$  or  $\beta_{\text{int}} = 0.62 \times 10^{-6} \text{sr}^{-1}$  column-integrated brightness. The peak  $\beta_{\text{int}}$  of  $14.2 \times 10^{-6} \text{sr}^{-1}$  was attained at 0:23 UT. The altitude-time section of the volume backscatter coefficient  $\beta$  is displayed in Fig. 2. Striking features are the thinness of the layer with 410 m average full-width half-maximum (FWHM, min: 180 m, max: 1.26 km) and its strong modulation in altitude as well as brightness.

The NLC layer is located between 79.5 and 82.8 km altitude. The mean centroid altitude  $z_c$  is 81.17 km with a standard deviation of 480 m due to oscillatory motions in the

vertical. The average descent rate of NLC particles between 21:59–1:49 UT is  $7.6\text{cm s}^{-1}$ , in accordance with the sedimentation velocity of large ice particles [Turco *et al.*, 1982]. No vertically separated NLC layers are detected. The general morphology of the cloud layer including the decline in brightness towards the end of the NLC observation is similar to NLC observed at polar latitudes. A detailed comparison with mid-latitude NLC statistics will be conducted in section 6.2.

### 3.2. Temperature during NLC event

The nightly mean temperature profile along with the static stability on the day of the NLC event are shown in Fig. 3a. The temperature minimum indicating the mesopause is found in the altitude range of 78–82 km with a minimum of 150 K at 80.5 km. It resides short below the NLC lower boundary. A secondary temperature minimum is located at 84 km, which is 1.7 km above the NLC top boundary. The NLC is located within a region with high static stability of  $N^2 > 5 \times 10^{-4} \text{s}^{-2}$  between 80.5 and 83 km.

Fig. 3b shows atmospheric temperature between 76–86 km altitude with a resolution of 15 min and 630 m. Temperatures are generally low enough to sustain NLC particles. Comparing the NLC contour with the volume of supersaturated air ( $T < 150$  K, in shades of blue color) reveals that the NLC layer resides in the upper part of this volume. The temperature 540 m above the NLC layer is 163 K, which is too high to sustain NLC. The top NLC contour follows the 155 K temperature isoline closely. The temperature gradient at the upper boundary of the NLC layer is 25 K/km on average. Inside the NLC layer, an average temperature of 146 K is derived from the interpolated backscatter profiles and possibly overestimated by 5–10 K (see above).

We will come back to this unusual thermal structure. At polar latitudes, the NLC layer is mostly found in the lower part of the saturated region, allowing for growth atop the observed layer and rapid sublimation at the bottom due to a negative temperature gradient. Obviously, in this mid-latitude event, these mechanisms are not at work, yet the environment allows for bright NLC displays by other means.

## 4. Analysis of local dynamics

### 4.1. Motions of NLC layer

Predominantly downward motions of the NLC layer occur during five periods with very similar descent rates between 0.55 and 0.71 m s<sup>-1</sup>. These are 20:21–20:37 UT, 22:19–23:03 UT, 0:03–0:23 UT, 0:33–0:53 UT, and 1:15–1:39 UT as indicated in Fig. 4a by red lines. We will show that these vertical motions match gravity wave signatures in the temperature field.

One-dimensional wavelet transformations of  $z_c(t)$  with a 6th order Morlet wavelet reveal vertical displacements with periods above 50 min (Fig. 4b). Another component with 30 to 80 min period is detected after 0:30 UT. Distinct oscillations at shorter time scales of 11 min occur between 22:45–23:30 UT. The shortest oscillation of 200 s between 0:30–1 UT has either been created by Doppler-shifting to periods below the Brunt-Vaisälä period, or either arose due to the interaction with an infrasonic wave [Pilger *et al.*, 2013]. The propagation of infrasonic waves along a mesospheric duct seems likely for the ambient atmospheric conditions described for this case. Variations in layer altitude are likely most strongly coupled to vertical winds.

Regarding brightness, one would expect an adaptation to the temperature field, although with a time lag. Wavelet analysis of  $\beta_{\max}(t)$  and the column-integrated quantity

$\beta_{\text{int}}(t)$  yields oscillations of brightness with a period of 50 min throughout the observation of the main NLC layer starting at 22:15 UT (Fig. 4c-f). These variations can only be induced by wave action along the trajectory of the ice particles. However, they were likely moderate with peak temperatures below 150 K, as for higher temperatures NLC particles would be quickly destroyed. Periods with oscillations at shorter time scales occur also between 0–1:30 UT.

## 4.2. Temperature perturbations

Fig. 4g shows time series of temperature at the centroid NLC altitude and  $\beta_{\text{int}}$  for comparison. Times with  $T < 150$  K (above the dashed line) indicating suitable conditions for NLC particle growth are found between 20:00–20:20 UT, 21:50–22:45 UT, and 23:15–1:30 UT. In accordance, these are also times with increasing NLC brightness. Spectral analysis reveals a tendency for temperature variations at periods above 90 min throughout the measurement. Interestingly, a 30–40 min oscillation dominates at times with weak brightness, while for the duration of the strongest NLC displays from 22:15 UT onwards, the temperature environment was stable with no perturbations at small scales. We note that the temporal resolution of temperature soundings is coarser than the NLC soundings, such that temperature variations at scales below 15 min cannot be resolved.

Temperature perturbations caused by gravity waves were also inferred from vertical temperature profiles by application of a 5th order Butterworth filter with 15 km cutoff vertical wavelength following *Ehard et al.* [2015]. Below the NLC layer down to 40 km, no dominant wave of significant amplitude stands out. Wave activity is most prominent in the mesopause region. This hints at wave activities within a region of high static

stability at NLC altitudes and a domination of horizontal over vertical propagation above the observation site.

At mesospheric altitudes, the wave field is complex with wave amplitudes above 20 K for both upward- and downward-slanted phase lines. NLC layers moving upward and downward at these time scales are often observed. To study the relation of these to the respective phases in the temperature field, a separation into quasi-horizontal waves and perturbations with downward and upward phase velocities using a two-dimensional wavelet analysis as employed by *Kaifler et al.* [2017] is presented in Fig. 5. We verified that the general structure of the waves' cold phases does not depend on the choice of interpolation method or resolution (not shown here). Two vertically stacked cold phases separated by 3 km are visible, where NLC populates the lower one (Fig. 5a). Upward- and downward slanted phase lines are found with periods of 20 to 90 min and observed phase velocities around  $0.65 \text{ m s}^{-1}$  throughout the mesosphere-lower thermosphere (MLT) region (Fig. 5b). Typical vertical wavelengths are 1–3 km.

The correlation between upward and downward motions of the NLC layer and the cold phases of gravity waves becomes obvious in Fig. 5b and c. Periods as well as vertical phase velocities observed in the temperature field match the simultaneous motions of the NLC layer, which is confined mostly to the cold phases of either upward- or downward-slanted waves. The beginning of the main NLC layer at 22 UT coincides with cold phases in Fig. 5b and c.

Beginning with the small-scale altitude variations around 23 UT, the column-integrated brightness remains low until 0 UT. The subsequent increase occurs either due to fast particle growth or due to arrival of a new population of ice particles in the lidar field

of view. To study the evolution of ice particles in the given environment, we employ a microphysical model. This will enable us to separate local effects from the effect of transport of particles through the lidar beam.

### 4.3. Microphysical evolution of NLC particles

For the first time, the Community Aerosol and Radiation Model for Atmospheres [CARMA *Turco et al.*, 1979; *Toon et al.*, 1979; *Turco et al.*, 1982; *Jensen and Thomas*, 1989; *Rapp and Thomas*, 2006] is driven with lidar temperature measurements for one-dimensional simulations. Within CARMA, ice particles form via heterogeneous nucleation and grow or sublimate according to the ambient conditions described by temperature and saturation. Ice particles are transported due to wind, vertical diffusion, and sedimentation.

In this study, the temperature is taken directly from the lidar measurements, however, no information about the vertical wind and humidity are available. We overcome this shortcoming by estimating the effective vertical wind from the temporal derivative of the centroid altitude of the NLC layer, which results in a combination of the sedimentation velocity and the vertical wind. We use this time series in CARMA for the vertical wind and in turn switch off sedimentation. The water vapor mixing ratio is chosen to be 5 ppm, but is varied to test the sensitivity.

The model is set up with 222 vertical grid boxes of 130 m thickness from 70 km to 90 km altitude. The ice particles are resolved in 28 size bins with mass doubling between subsequent bins. The smallest bin corresponds to ice particles of 2 nm radius. Profiles for temperature and values for the vertical wind are updated every 5 min.

CARMA simulations without an initial NLC population indeed show evidence of ice particle nucleation in regions with the lowest temperature (at 20:15 UT, 22:20 UT and 1:50 UT, not shown). However, the environment does not favour growth to sizes visible to the lidar. Therefore we chose to initialize the simulation at 22 UT with a population of 33 particles per cubic centimeter of 42 nm mean radius following a Gaussian size distribution of 15 nm width according to *Baumgarten et al.* [2008, their Table 3, faint NLC]. The initial vertical extent of the simulated NLC is 540 m which corresponds to six grid cells. This defines the backscatter coefficient at 22 UT to be  $\beta = 3 \times 10^{-10} \text{m}^{-1} \text{sr}^{-1}$  according to the observation and simulates the arrival of particles in the field of view of the lidar at this time.

In a run including diffusion, NLC particles quickly spread within the supersaturated altitude range in contrast to the measurements, where the layer resides in the upper part of the region. This hints at strongly reduced diffusion corresponding to very low levels of mesospheric turbulence. *Rapp and Thomas* [2006] found that in the absence of diffusion, NLC particles develop to large radii with very narrow size distribution, and attain large values of volume backscatter coefficient, which is in concordance with our observation of an unusually bright cloud at this latitude. We subsequently disable diffusion, essentially fixing the layer in its width as well.

Fig. 6 shows the simulated brightness, ice particle number density, and mean radius of the ice particles. The particle radii vary in a reasonable range without total sublimation, indicating a general equilibrium with the local temperatures. Although the ice particle number density gradually decreases (as particles can only sublimate, but not be generated), the effective backscatter coefficient attains values in the same range as the ob-



servations even four hours after initialization. This means that the local environment, although unable to create visible NLC from nucleation, is very well able to sustain an already developed particle population. At the same time this result demonstrates the overall consistency of the absolute temperatures within the NLC layer. A decrease of temperatures by only 1 K resulted in unrealistically large backscatter coefficients, while in a warmer environment ice particles quickly sublimated.

A comparison of simulated and observed maximum brightness is shown in Fig. 7, together with temperature at the NLC centroid altitude on an inverse scale. Conjointly with the measurements, the simulated brightness starts to increase from 22 UT. Higher  $\beta$  is attained, and the subsequent decrease due to increasing temperature sets in later. Both model and observations yield similar results in the period with low brightness from 23 UT to 23:45 UT. The sudden increase in observed  $\beta$  at 0 UT, however, is not simulated. Here, ice particles grow considerably slower, maximizing at 2 UT, when the observed layer has already faded. Neither a decrease in temperature (not shown) nor an increase in water vapour can reproduce the observed increase at 0 UT and decrease at 1:30 UT, leading us to the conclusion that at 0 UT new particles were transported into the beam.

After 1:20 UT, the observed  $\beta$  decreases when the local conditions would have allowed for significant increase. So the NLC display did not fade because the particles sublimated, but rather because they were transported out of the beam and no new particles followed. The same likely happened at 20 UT, when the temperature was even lower, but the NLC was only weak and subsided. The evolution of NLC brightness is governed by the ambient conditions the ice particles were exposed to along their trajectory, taking into account the relevant time scales. In a gravity-wave-perturbed environment, this is determined by

the relative motions between the advected ice particles and the horizontal phase speeds of the waves that modulate the temperature. While high temperatures destroy NLC effectively, the CARMA simulations show that few hours are sufficient for growth from very weak to the observed maximum brightness displays. It is therefore also possible for NLC generation or re-generation along the trajectory in suitable conditions, i.e., ice particles moving within the cold phases of gravity waves.

## **5. Evidence for horizontal transport of ice particles**

Besides the presented lidar soundings of NLC particles, additional information on mesospheric ice particles during this event comes from (1) meteor radars providing mesospheric wind to trace the path of NLC particles, (2) the NLC-viewing camera CIPS on the AIM satellite, (3) the VHF radar OSWIN located in Kühlungsborn, (4) various north-pointing photo cameras at stations in the northern Alps and the Bavarian Forest, and (5) ground-based observers throughout central and northern Europe.

### **5.1. Winds by meteor radar**

Information on winds in the MLT region between 78–106 km is obtained from two meteor radars located in Juliusruh, 640 km north of the CORAL lidar [Stober *et al.*, 2012, 2017] and Collm, 270 km north of CORAL [Jacobi *et al.*, 2007; Jacobi, 2012]. Altitude-time sections of both the zonal and meridional wind show signatures of a strong quasi 2-day planetary wave (Fig. 8). Wavelet analysis with a 6th-order Morlet wavelet of time series at 82 km altitude of both zonal and meridional wind reveal a dominant period around 48 h (Fig. 9). Such quasi 2-day planetary waves are frequent phenomena in the summer mid-latitude MLT [e.g. Lilienthal and Jacobi, 2015]. On 18 July 2016, strong southward

winds thus allowed for the inflow of cold polar air masses to mid-latitudes. Daily median wind values corrected for gravity wave and tidal perturbations by means of an adaptive spectral filter are tabulated in Table 1. The average wind speed at 82 km altitude is thus  $\approx 22 \text{ m s}^{-1}$  or  $80 \text{ km h}^{-1}$  in mainly southward direction. On 19 July, the meridional wind direction reverses, presumably stopping the supply of NLC particles from the north. During the time of the NLC observation, the zonal wind reversal is found at 83 km altitude, directly above the NLC layer.

## 5.2. CIPS imagery

The CIPS camera onboard the AIM satellite detected an extended region of NLC between  $52^\circ\text{N}$  and  $62^\circ\text{N}$  (1500 km latitudinal extent) during orbit 50455 on 18 July 2016 at 16:06 UT above the North Sea (Fig.10). This event was one of the two southern-most observations in this season with the other one occurring on 14/15 July around  $170^\circ\text{E}$  longitude. Only on five other days NLC were detected south of  $60^\circ\text{N}$ . On 18 July, a series of prominent wave fronts with spatial distances of 300 and 380 km aligned in south-west to north-east direction are visible. Were these wave crests transported above a ground-based station in this configuration with the wind speed derived from the meteor radar observations, they would map to periods of 4-5 h. CIPS also shows aligned wave crests with about 80 km (mapping to 1 h) distance. Due to different requirements for lighting conditions (CORAL operates in darkness, while CIPS detects reflected sunlight), a closer coincidence between CIPS and CORAL measurements is impossible. The previous orbit strip in the region also showed high albedo above Finland at 14:30 UT on 18 Jul 2016, and absence of NLC southwards until Italy.

### 5.3. Mesospheric summer echoes

Mesospheric summer echoes (MSE) were recorded by the OSWIN VHF radar in Kühlungsborn (54.12°N, 11.77°E, 605 km north of CORAL) between 9–19 UT on 18 Jul 2016 (Fig.11). However, local Rayleigh lidar measurements were prevented by tropospheric clouds. The MSE layer was detected in the altitude range of 81–85 km. Its structure resembles the NLC layer structure (Fig.2) observed about 11 h later and 600 km towards the south. Transport of ice particles from the latitude of the radar to the latitude of the lidar observation is expected to take 7–8 h using the wind speed estimated above. A descent of 1.5–2 km of this layer of ice particles between the observations at Kühlungsborn and the Bavarian Forest is reasonable for typical sedimentation velocities of few  $\text{cm s}^{-1}$ . Although it is unlikely that these were soundings of the very same volume, the overall resemblance is remarkable given the typical geophysical variability of cloud layers, and indicates the existence of an extended, coherent wave field.

### 5.4. Visual observations

Despite cloudy conditions in some parts of central Europe, visual confirmation of NLC above Europe is reported in the evening of 18 July and the morning of 19 July from Germany, Poland, Latvia, Estonia, Norway, and Finland by amateur observers [spaceweather.com] northwards of 50°N. An automated camera network [<http://www.foto-webcam.eu>] observed NLC from seven stations in the Alps and Bavarian Forest (e.g. from Brauneck, Herzogstand, Grosser Arber, and Munich city). Twilight conditions allowed for visual observations from Germany's southern border between 19:30–21:00 on 18 July 2016 and between 1:30–3:00 UT on 19 July 2016 when the sun was between  $-5$  to  $-15^\circ$  below the horizon. Visual NLC observations were reported between 20:10–20:50 UT and

between 1:50–2:10 UT. Typically, the location of NLC observed close to the horizon maps to 300–1000 km distance from the observer along the viewing direction. Thus, the NLC observed by these cameras maps to the central part of Germany.

Based on the observational evidence presented in the previous sections, we conclude that this NLC event was strong and wide-spread over central and northern Europe. From MLT wind measurements and CIPS imagery, it is deduced that ice particles were transported from higher latitudes to the observation site.

## **6. Implications for mid-latitude NLC**

The question remains to what extent this case is typical for mid-latitude NLC. In the following, after a comparison to the thermal environment at polar latitudes, we attempt a comparison with statistics of mid-latitude NLC and evaluate the thermal structure of mid-latitude summer in central Europe.

### **6.1. Relation to NLC at polar latitudes**

The nightly mean temperature profile (Fig. 3a) differs significantly from what is known about the thermal structure in the vicinity of NLC at polar latitudes, an environment that naturally sustains the nucleation and growth of ice particles [see *Rapp and Lübken, 2004*, their Fig. 1]. There, the temperature minimum is located 6 km above the NLC layer, which is deduced from rocket and lidar [*Lübken et al., 2004*, their Fig. 4 and 11] as well as satellite soundings [*Hultgren and Gumbel, 2014*]. The altitude difference between the temperature minimum and the NLC peak is of vital importance for the microphysical evolution of NLC particles. Growth of NLC particles to visible sizes occurs within few hours during their descent from their altitude of nucleation around the mesopause. In

our case at mid-latitudes, no such altitude range suitable for NLC particle growth exists.

It is therefore safe to conclude that the detected NLC particles did not originate at this location but are transported to the observation site by meridional winds.

At polar latitudes, the sublimation of NLC particles at the lower boundary occurs due to a negative temperature gradient. Here, this is not generally the case. For example at 22:20 and 1 UT, temperatures stay well below 150 K for almost 2 km below the NLC lower boundary. Here the reduced diffusion confines the NLC particles to a thin layer that does not sediment into cold regions before it is transported out of the lidar beam.

The strong variations in NLC brightness hint at the action of gravity waves along the trajectory. *Rapp et al.* [2002] studied the evolution of NLC particles subjected to perturbations caused by gravity waves. For wave periods below 3 h, they found reduced NLC brightness compared to a wave-free reference case. This might not apply to mature NLC particles as in our case to the same extent. Yet it is an indication that the dominant gravity wave intrinsic periods are above 3 h. In such conditions, also the CARMA simulations predict growth of ice particles to radii matching the observed brightness.

## **6.2. Comparison to mid-latitude NLC statistics and relation to temperatures**

With a centroid altitude of 81.2 km, the observed NLC resides in the lower range of NLC centroid altitudes typical for mid-latitudes. The mean centroid altitude of 82.3 km from 15 years of lidar measurements at 54°N by *Gerding et al.* [2013] is significantly higher than our observation, as is the altitude of 82.4 km extrapolated to 49°N from *Chu et al.* [2011]. With a maximum volume backscatter coefficient of  $\beta = 12 \times 10^{-10} \text{ m}^{-1}\text{sr}^{-1}$ , the NLC is exceptionally bright given the latitude. *Gerding et al.* [2013] listed only 0.1–0.5 % of all NLC at 54°N to be as bright or brighter than  $12 \times 10^{-10} \text{ m}^{-1}\text{sr}^{-1}$ . At the same time, an

enhanced brightness is in concordance with the low altitude, as is the low FWHM. With a 410 m FWHM, the thickness of the layer is at the minimum level given by *Gerding et al.* [2013, their Fig. 6]. For 69°N, *Kaifler et al.* [2011] listed significantly wider layers (1.68 km vertical extent versus 900 m reported here). In terms of vertical displacement, downward progression, and mean duration, this NLC event yields similar values as observed at 69°N and 69°S [*Kaifler et al.*, 2013].

The event observed on 18/19 July 2016 exhibited an unusually long duration of 4.9 h, and it was the only NLC event observed by CORAL during this season. The only other NLC event detected above southern Germany by the camera network in this season occurred in the evening of 5 July from a location close to CORAL. On this day, temperatures below 150 K were recorded for a short time span of 1.5 h but no NLC was detected by the lidar. Thus, the southern boundary of this visually observed cloud was located in the north of CORAL.

The temperature profile obtained during the night of NLC observation deviates significantly from the climatological mean for this location. The temperature minimum is found almost 30 K and 6 km below the average for July as observed by SABER (with the NLC sounding excluded, Fig. 12a). The climatological temperature lies above 170 K at the time and location of this NLC event (Fig. 12b). It also shows that the temperature at NLC altitudes above GERES station is significantly higher than that above Kühlungsborn. Therefore, an extreme event in terms of temperature perturbations was necessary to facilitate NLC occurrence above GERES station.

## 7. Conclusions

On 18/19 July 2016, the atmospheric state of the MLT region at 48.8°N in southern Germany was dominated by a stable, strong vertical temperature gradient at the mesopause that defined an upper limit for the existence of NLC particles. The action of a quasi 2-day planetary wave forced cold mesospheric polar air towards mid-latitudes, carrying NLC particles whose lifetime was prolonged due to reduced diffusion, i.e., low levels of mesospheric turbulence. This firstly confined the particles to a very narrow altitude range, such that the NLC layer stayed very thin at high brightness. Secondly, the warming of the ambient air due to mixing with warmer air above was inhibited. Simulations with a microphysical model showed that NLC particles were able to survive in the observed local environment.

The presented case arose due to an extreme event driving the conditions in the MLT region far from the climatological mean. The fact that in the 2016 season a single extreme event occurred above GERES station rather than many weak events, as seems to be the case at Kühlungsborn, speaks for the relevance of this particular mechanism. Although advection of particles plays a major role, the observations and simulations shown here stress the importance of the local conditions along the trajectory and above the observation site, as they facilitate the survival and growth of the advected particles.

### **Acknowledgments.**

The research leading to these results was performed within the ARISE2 project ([www.ARISE-project.eu](http://www.ARISE-project.eu)) and received funding from the European Community's Horizon 2020 programme under grant agreement 653980. NK was supported by the Helmholtz association in the project PD-206. Lidar data is available on the HALO-DB at <https://halo->



db.pa.op.dlr.de/mission/110. We thank Cora Randall for contributing CIPS data. CIPS data is available online at <http://lasp.colorado.edu/aim/index.html>. We thank the SABER scientific team for the access to their online database at <http://saber.gats-inc.com/index.php>.

## References

- Baumgarten, G., J. Fiedler, F.-J. Lübken, and G. von Cossart (2008), Particle properties and water content of noctilucent clouds and their interannual variation, *Journal of Geophysical Research: Atmospheres*, *113*(D6), n/a–n/a, doi:10.1029/2007JD008884, d06203.
- Christensen, O. M., P. Eriksson, J. Urban, D. Murtagh, K. Hultgren, and J. Gumbel (2015), Tomographic retrieval of water vapour and temperature around polar mesospheric clouds using Odin-SMR, *Atmospheric Measurement Techniques*, *8*(5), 1981–1999, doi:10.5194/amt-8-1981-2015.
- Christensen, O. M., S. Benze, P. Eriksson, J. Gumbel, L. Megner, and D. P. Murtagh (2016), The relationship between polar mesospheric clouds and their background atmosphere as observed by Odin-SMR and Odin-OSIRIS, *Atmospheric Chemistry and Physics*, *16*(19), 12,587–12,600, doi:10.5194/acp-16-12587-2016.
- Chu, X., W. Huang, W. Fong, Z. Yu, Z. Wang, J. A. Smith, and C. S. Gardner (2011), First lidar observations of polar mesospheric clouds and Fe temperatures at McMurdo (77.8°S, 166.7°E), Antarctica, *Geophysical Research Letters*, *38*(16), n/a–n/a, doi:10.1029/2011GL048373, l16810.

- Ehard, B., B. Kaifler, N. Kaifler, and M. Rapp (2015), Evaluation of methods for gravity wave extraction from middle-atmospheric lidar temperature measurements, *Atmospheric Measurement Techniques*, 8(11), 4645–4655, doi:10.5194/amt-8-4645-2015.
- Fiedler, J., G. Baumgarten, U. Berger, P. Hoffmann, N. Kaifler, and F.-J. Lübken (2011), NLC and the background atmosphere above ALOMAR, *Atmospheric Chemistry and Physics*, 11(12), 5701–5717, doi:10.5194/acp-11-5701-2011.
- Fogle, B. (1966), Recent advances in research on noctilucent clouds, *Bull. Amer. Meteorol. Soc.*, 47(10), 781–787.
- Gerding, M., J. Höffner, and M. Rauthe (2007a), Simultaneous observations of temperatures and ice-particles in the mid-latitude mesopause region, *Advances in Space Research*, 40(6), 785 – 793, doi:http://dx.doi.org/10.1016/j.asr.2007.01.020.
- Gerding, M., J. Höffner, M. Rauthe, W. Singer, M. Zecha, and F.-J. Lübken (2007b), Simultaneous observation of noctilucent clouds, mesospheric summer echoes, and temperature at a midlatitude station (54°N), *Journal of Geophysical Research: Atmospheres*, 112(D12), n/a–n/a, doi:10.1029/2006JD008135, d12111.
- Gerding, M., J. Höffner, P. Hoffmann, M. Kopp, and F.-J. Lübken (2013), Noctilucent cloud variability and mean parameters from 15 years of lidar observations at a mid-latitude site (54°N, 12°E), *Journal of Geophysical Research: Atmospheres*, 118(2), 317–328, doi:10.1029/2012JD018319.
- Hauchecorne, A., and M.-L. Chanin (1980), Density and temperature profiles obtained by lidar between 35 and 70 km, *Geophysical Research Letters*, 7(8), 565–568, doi:10.1029/GL007i008p00565.

Hervig, M. E., M. H. Stevens, L. L. Gordley, L. E. Deaver, J. M. Russell, and S. M. Bailey (2009), Relationships between polar mesospheric clouds, temperature, and water vapor from solar occultation for ice experiment (SOFIE) observations, *Journal of Geophysical Research: Atmospheres*, *114*(D20), n/a–n/a, doi:10.1029/2009JD012302, d20203.

Hervig, M. E., M. Gerding, M. H. Stevens, R. Stockwell, S. M. Bailey, J. M. R. III, and G. Stober (2016), Mid-latitude mesospheric clouds and their environment from SOFIE observations, *Journal of Atmospheric and Solar-Terrestrial Physics*, *149*, 1 – 14, doi: <http://dx.doi.org/10.1016/j.jastp.2016.09.004>.

Hultgren, K., and J. Gumbel (2014), Tomographic and spectral views on the lifecycle of polar mesospheric clouds from Odin/OSIRIS, *Journal of Geophysical Research: Atmospheres*, *119*(24), 14,129–14,143, doi:10.1002/2014JD022435, 2014JD022435.

Hultgren, K., H. Kőrnic, J. Gumbel, M. Gerding, P. Hoffmann, S. Lossow, and L. Megner (2011), What caused the exceptional mid-latitudinal noctilucent cloud event in July 2009?, *Journal of Atmospheric and Solar-Terrestrial Physics*, *73*(14), 2125 – 2131, doi:<http://doi.org/10.1016/j.jastp.2010.12.008>, Layered Phenomena in the Mesopause Region.

Jacobi, C. (2012), 6 year mean prevailing winds and tides measured by VHF meteor radar over Collm (51.3° N, 13.0° E), *Journal of Atmospheric and Solar-Terrestrial Physics*, *78*, 8 – 18, doi:<http://dx.doi.org/10.1016/j.jastp.2011.04.010>, Structure and Dynamics of Mesosphere and Lower Thermosphere.

Jacobi, C., K. Fröhlich, C. Viehweg, G. Stober, and D. Kürschner (2007), Mid-latitude mesosphere/lower thermosphere meridional winds and temperatures measured with meteor radar, *Advances in Space Research*, *39*(8), 1278 – 1283, doi:

<http://dx.doi.org/10.1016/j.asr.2007.01.003>.

Jensen, E., and G. E. Thomas (1989), On the diurnal Variation of Noctilucent Clouds, *J. Geophys. Res.*, *94*(D12), 14,693–14,702.

Kaifler, N., G. Baumgarten, J. Fiedler, R. Latteck, F.-J. Lübken, and M. Rapp (2011), Coincident measurements of pmse and NLC above ALOMAR (69°N, 16°E) by radar and lidar from 1999-2008, *Atmospheric Chemistry and Physics*, *11*(4), 1355–1366, doi:10.5194/acp-11-1355-2011.

Kaifler, N., G. Baumgarten, and J. Fiedler (2013), Quantification of waves in lidar observations of noctilucent clouds at scales from seconds to minutes, *Atmospheric Chemistry and Physics*, *13*(23), 11,757–11,768, doi:10.5194/acp-13-11757-2013.

Kaifler, N., B. Kaifler, B. Ehard, S. Gisinger, A. Dörnbrack, M. Rapp, R. Kivi, A. Kozlovsky, M. Lester, and B. Liley (2017), Observational indications of downward-propagating gravity waves in middle atmosphere lidar data, *Journal of Atmospheric and Solar-Terrestrial Physics*, *162*, 16 – 27, doi:<http://doi.org/10.1016/j.jastp.2017.03.003>,  
layered Phenomena in the Mesopause Region.

Kiliani, J., G. Baumgarten, F.-J. Lübken, U. Berger, and P. Hoffmann (2013), Temporal and spatial characteristics of the formation of strong noctilucent clouds, *Journal of Atmospheric and Solar-Terrestrial Physics*, *104*, 151–166, doi:10.1016/j.jastp.2013.01.005.

Lilienthal, F., and C. Jacobi (2015), Meteor radar quasi 2-day wave observations over 10 years at Collm (51.3° N, 13.0° E), *Atmospheric Chemistry and Physics*, *15*(17), 9917–9927, doi:10.5194/acp-15-9917-2015.

Lübken, F.-J., K.-H. Fricke, and M. Langer (1996), Noctilucent clouds and the thermal structure near the arctic mesopause in summer, *Journal of Geophysical Research: At-*

*mospheres*, 101(D5), 9489–9508, doi:10.1029/96JD00444.

Lübken, F.-J., M. Zecha, J. Höffner, and J. Röttger (2004), Temperatures, polar mesosphere summer echoes, and noctilucent clouds over Spitsbergen (78°N), *Journal of Geophysical Research D: Atmospheres*, 109(11), D11,203 1–14, doi:10.1029/2003JD004247.

Nielsen, K., G. E. Nedoluha, A. Chandran, L. C. Chang, J. Barker-Tvedtnes, M. J. Taylor, N. J. Mitchell, A. Lambert, M. J. Schwartz, and J. M. R. III (2011), On the origin of mid-latitude mesospheric clouds: The July 2009 cloud outbreak, *Journal of Atmospheric and Solar-Terrestrial Physics*, 73(14), 2118 – 2124, doi: <http://dx.doi.org/10.1016/j.jastp.2010.10.015>, layered Phenomena in the Mesopause Region.

Pilger, C., C. Schmidt, and M. Bittner (2013), Statistical analysis of infrasound signatures in airglow observations: Indications for acoustic resonance, *Journal of Atmospheric and Solar-Terrestrial Physics*, 93, 70 – 79, doi:<https://doi.org/10.1016/j.jastp.2012.11.011>.

Plane, J. M. C., B. J. Murray, X. Chu, and C. S. Gardner (2004), Removal of meteoric iron on polar mesospheric clouds, *Science*, 304(5669), 426–428, doi:10.1126/science.1093236.

Rapp, M., and F.-J. Lübken (2004), Polar mesosphere summer echoes (PMSE): Review of observations and current understanding, *Atmospheric Chemistry and Physics*, 4(11/12), 2601–2633, doi:10.5194/acp-4-2601-2004.

Rapp, M., and G. E. Thomas (2006), Modeling the microphysics of mesospheric ice particles: Assessment of current capabilities and basic sensitivities, *Journal of Atmospheric and Solar-Terrestrial Physics*, 68(7), 715 – 744, doi: <http://dx.doi.org/10.1016/j.jastp.2005.10.015>.

Rapp, M., F.-J. Lübken, A. Müllemann, G. E. Thomas, and E. J. Jensen (2002), Small-scale temperature variations in the vicinity of NLC: Experimental and model results, *Journal of Geophysical Research: Atmospheres*, 107(D19), AAC 11–1–AAC 11–20, doi:10.1029/2001JD001241, 4392.

Rong, P. P., J. M. Russell, M. E. Hervig, and S. M. Bailey (2012), The roles of temperature and water vapor at different stages of the polar mesospheric cloud season, *Journal of Geophysical Research: Atmospheres*, 117(D4), doi:10.1029/2011JD016464, d04208.

Russell, J. M., P. Rong, M. E. Hervig, D. E. Siskind, M. H. Stevens, S. M. Bailey, and J. Gumbel (2014), Analysis of northern midlatitude noctilucent cloud occurrences using satellite data and modeling, *Journal of Geophysical Research: Atmospheres*, 119(6), 3238–3250, doi:10.1002/2013JD021017, 2013JD021017.

Russell III, J. M., M. G. Mlynczak, and L. L. Gordley (1994), Overview of the sounding of the atmosphere using broadband emission radiometry (SABER) experiment for the Thermosphere-Ionsphere-Mesosphere Energetics and Dynamics (TIMED) mission, doi:10.1117/12.187579.

Stober, G., C. Jacobi, V. Matthias, P. Hoffmann, and M. Gerding (2012), Neutral air density variations during strong planetary wave activity in the mesopause region derived from meteor radar observations, *Journal of Atmospheric and Solar-Terrestrial Physics*, 74, 55 – 63, doi:http://dx.doi.org/10.1016/j.jastp.2011.10.007.

Stober, G., V. Matthias, C. Jacobi, S. Wilhelm, J. Höffner, and J. L. Chau (2017), Exceptionally strong summer-like zonal wind reversal in the upper mesosphere during winter 2015/16, *Ann. Geophys.*, 35(3), 711–720, doi:10.5194/angeo-35-711-2017.

- Suzuki, H., K. Sakanoi, N. Nishitani, T. Ogawa, M. K. Ejiri, M. Kubota, T. Kinoshita, Y. Murayama, and Y. Fujiyoshi (2016), First imaging and identification of a noctilucent cloud from multiple sites in Hokkaido (43.2–44.4°N), Japan, *Earth, Planets and Space*, *68*(1), 182, doi:10.1186/s40623-016-0562-6.
- Thayer, J. P., N. Nielsen, and J. Jacobsen (1995), Noctilucent cloud observations over Greenland by a Rayleigh lidar, *Geophysical Research Letters*, *22*(21), 2961–2964, doi:10.1029/95GL02126.
- Theon, J. S., W. Nordberg, and W. S. Smith (1967), Temperature measurements in noctilucent clouds, *Science*, *157*(3787), 419–421, doi:10.1126/science.157.3787.419.
- Thomas, G. E. (1991), Mesospheric clouds and the physics of the mesopause region, *Reviews of Geophysics*, *29*(4), 553–575, doi:10.1029/91RG01604.
- Toon, O. B., R. P. Turco, P. Hamill, C. S. Kiang, and R. C. Whitten (1979), A one-dimensional model describing aerosol formation and evolution in the stratosphere: II. Sensitivity studies and comparison with observations, *J. Atmos. Sci.*, *36*(4), 718–736, doi:10.1175/1520-0469(1979)036<0718:AODMDA>2.0.CO;2.
- Turco, R. P., P. Hamill, O. B. Toon, R. C. Whitten, and C. S. Kiang (1979), A one-dimensional model describing aerosol formation and evolution in the stratosphere: I. Physical processes and mathematical analogs, *J. Atmos. Sci.*, *36*(4), 699–717, doi:10.1175/1520-0469(1979)036<0699:AODMDA>2.0.CO;2.
- Turco, R. P., O. B. Toon, R. C. Whitten, R. G. Keese, and D. Hollenbach (1982), Noctilucent clouds: Simulation studies of their genesis, properties and global influences, *Planet. Space Sci.*, *30*(11), 1147–1181, doi:10.1016/0032-0633(82)90126-X.

von Cossart, G., P. Hoffmann, U. von Zahn, P. Keckhut, and A. Hauchecorne (1996), Mid-latitude noctilucent cloud observations by lidar, *Geophysical Research Letters*, *23*(21), 2919–2922, doi:10.1029/96GL02768.

Wickwar, V. B., M. J. Taylor, J. P. Herron, and B. A. Martineau (2002), Visual and lidar observations of noctilucent clouds above Logan, Utah, at 41.7°N, *Journal of Geophysical Research: Atmospheres*, *107*(D7), ACL 2–1–ACL 2–6, doi:10.1029/2001JD001180.



**Table 1.** Winds from meteor radar above Juliusruh and Collm on 18 July 2016. Calculated propagation directions are clockwise from the north.

Site	Altitude (km)	Zonal wind $u$ (m/s)	Meridional wind $v$ (m/s)	Propagation direction (deg)
Juliusruh	80	$-19.1 \pm 0.9$	$-20.1 \pm 0.9$	224
Collm	80	$-11.2 \pm 0.9$	$-19.5 \pm 0.9$	210
Juliusruh	82	$-18.1 \pm 0.9$	$-22.5 \pm 0.9$	219
Collm	82	$-4.1 \pm 0.9$	$-21.6 \pm 0.8$	191
Juliusruh	84	$-11.8 \pm 0.8$	$-21.0 \pm 0.8$	209
Collm	84	$5.4 \pm 0.8$	$-22.6 \pm 0.8$	167

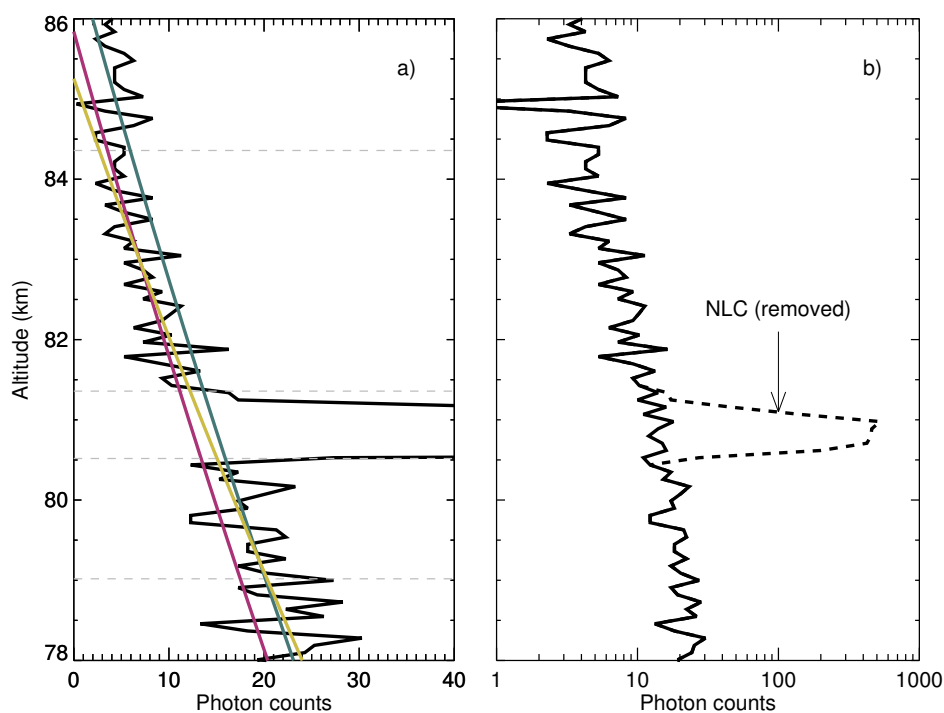


**Figure 1.** a) Photon count profile (black) at 0:59-1:00 UT on 19 July 2016. The colored lines represent fits to the region above (purple), below (blue) and both (yellow). Horizontal dashed lines mark the boundaries of the fit intervals. b) The original profile (dashed line) and the profile with NLC removed (solid). See text for details.

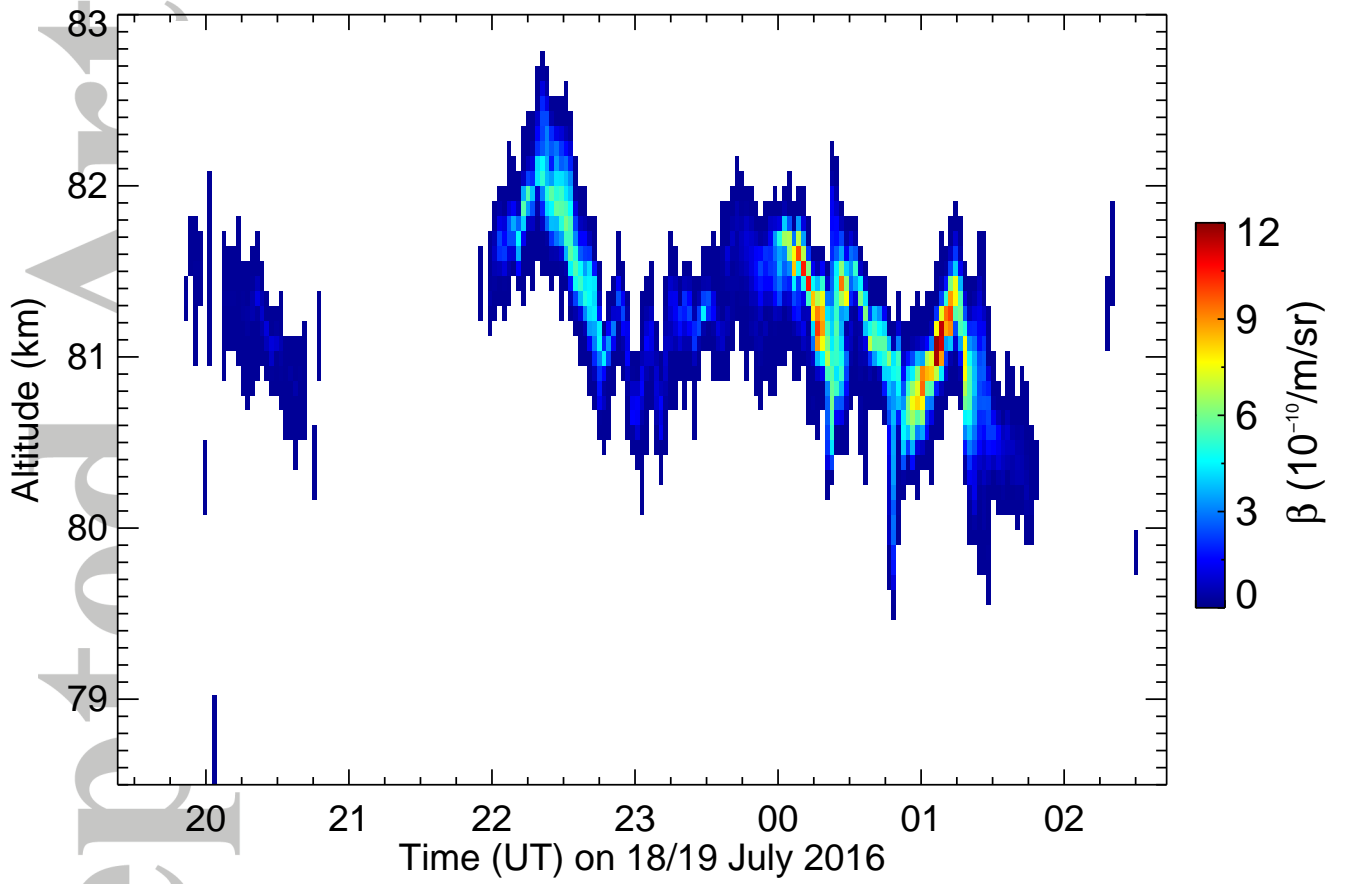


**Figure 2.** Altitude-time section of NLC volume backscatter coefficient  $\beta$  over GERES station (48.8°N) on 18/19 July 2016.

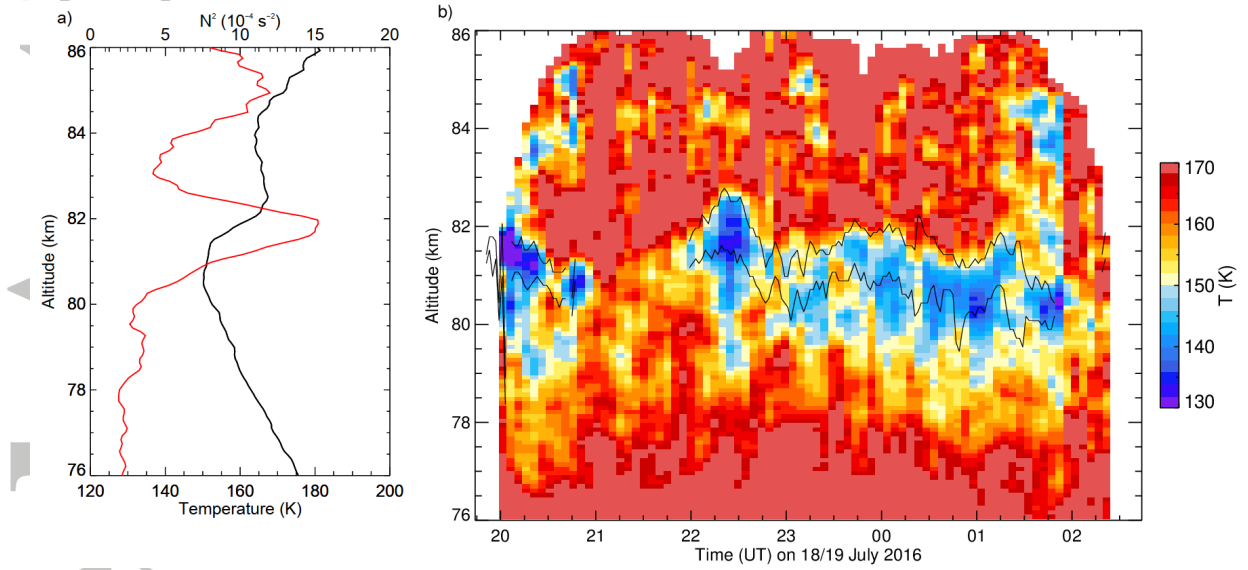


**Figure 3.** (a) Nightly mean temperature profile on 18/19 July 2016 (black) and corresponding static stability (red). (b) Altitude-time section of temperature measurements  $T(z, t)$  in the MLT region. The black contour indicates NLC top and bottom boundaries. Temperatures exceeding 170 K are colored light red.

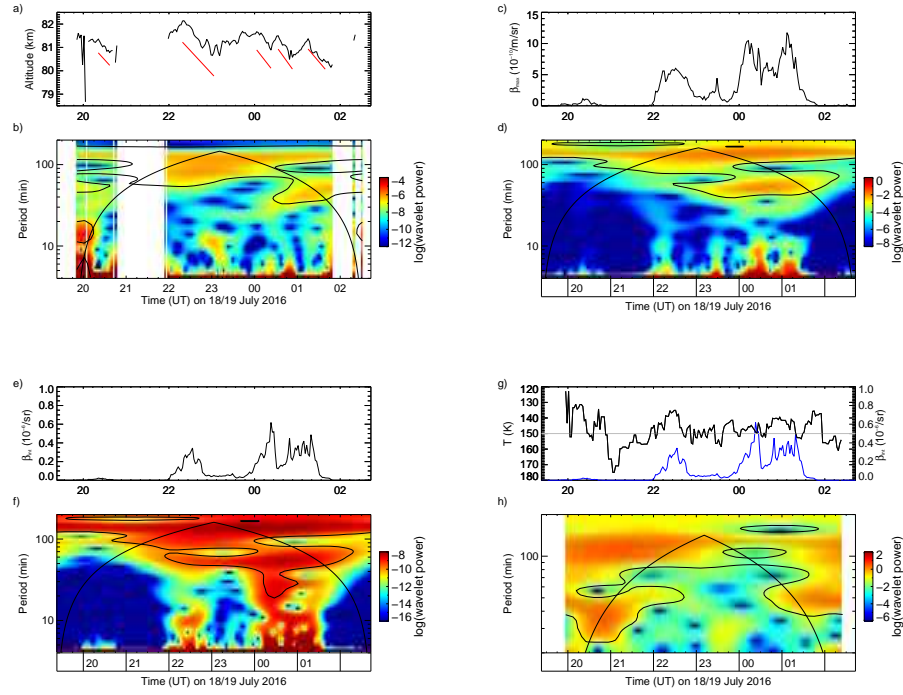


**Figure 4.** (a,b) Time series of NLC centroid altitude and its corresponding wavelet power spectrum. The black lines in (b) indicate the cone of influence and the 95 % significance level. (c,d) Same for  $\beta_{\max}(t)$ . (e,f) Same for column-integrated  $\beta_{\text{int}}(t)$ . (g,h) Same for temperature at centroid altitude. The integrated brightness is shown in blue for comparison (right axis). The grey line indicates  $T = 150$  K. Note the inversed temperature axis on the left.

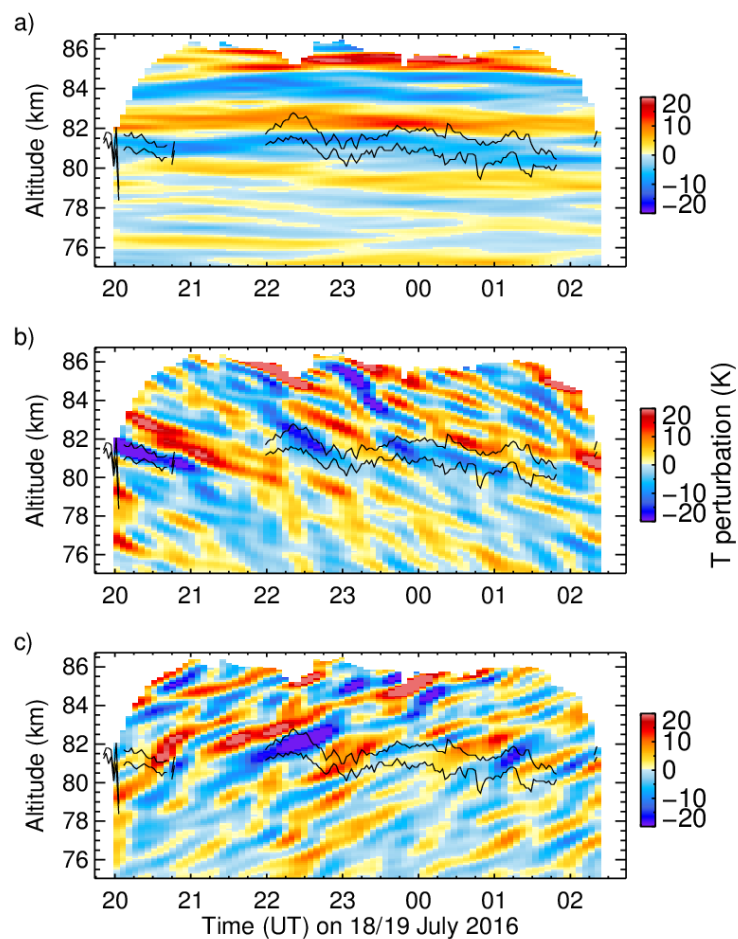


**Figure 5.** Reconstructed (a) quasi-horizontal waves, (b) waves with downward phase velocity, (c) waves with upward phase velocity.

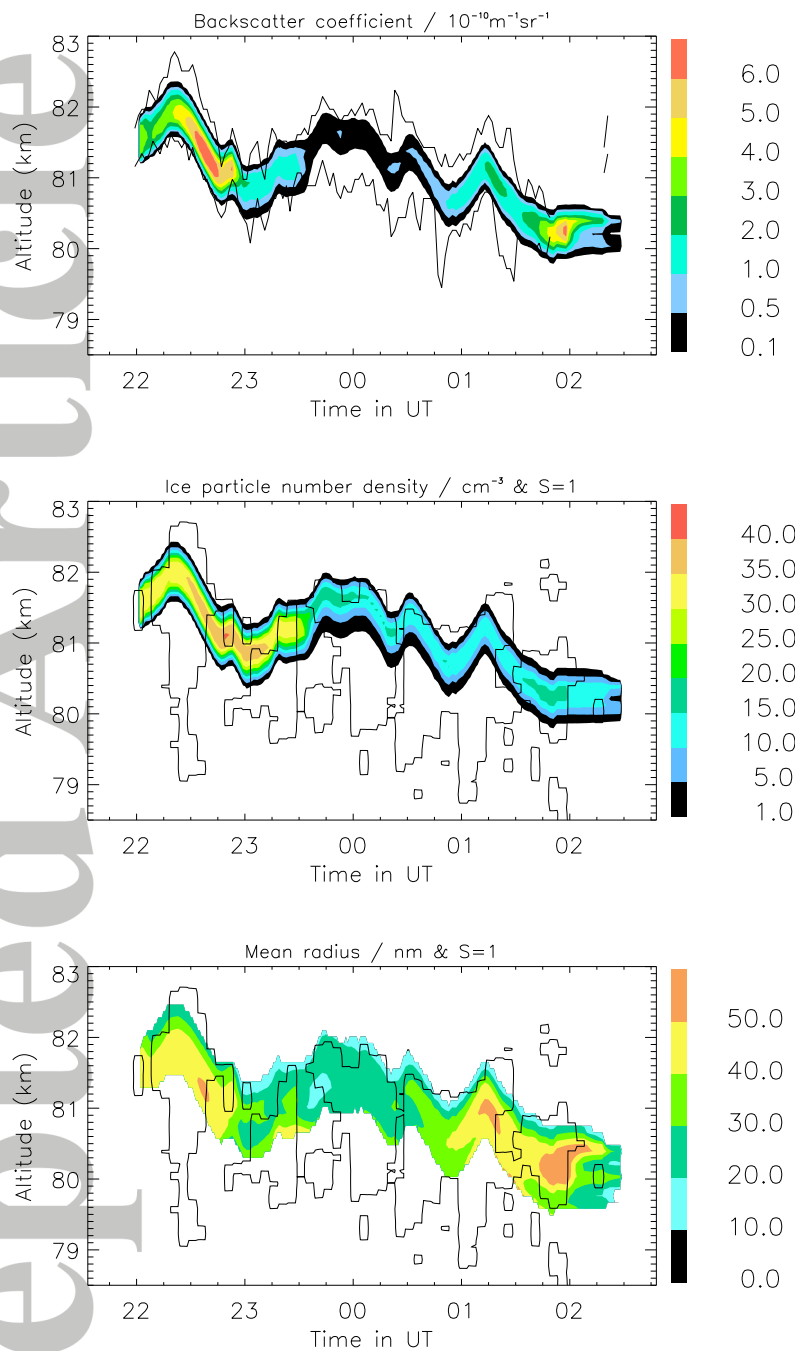


**Figure 6.** Time-altitude sections of CARMA-simulated (top) backscatter coefficient and lidar NLC contour, (center) ice particle number density and (bottom) mean radius as well as supersaturated area (contour) in a 5 ppm environment.

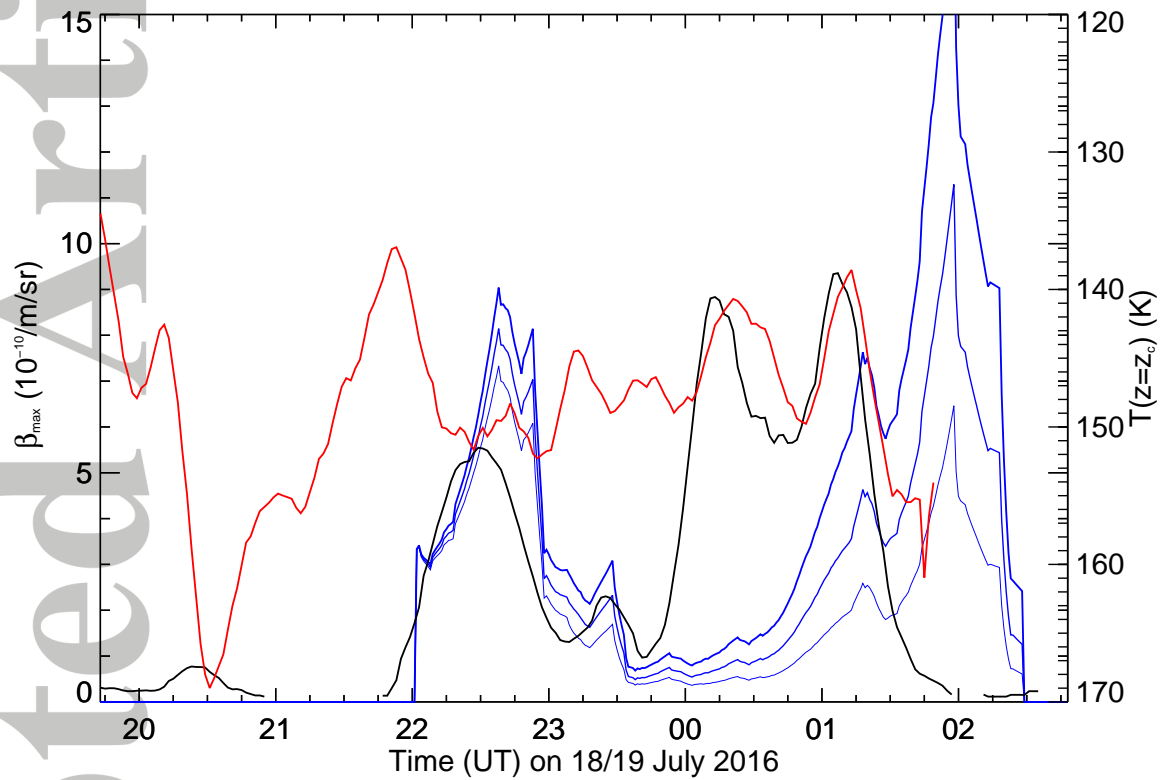


**Figure 7.** Comparison of CARMA simulations of  $\beta_{\max}(t)$  (blue for water vapour mixing ratios of 5, 5.5, and 6 ppm from low to high values) with  $\beta_{\max}(t)$  (black, smoothed to 15 min) and  $T(z = z_c, t)$  (red) measured by CORAL.



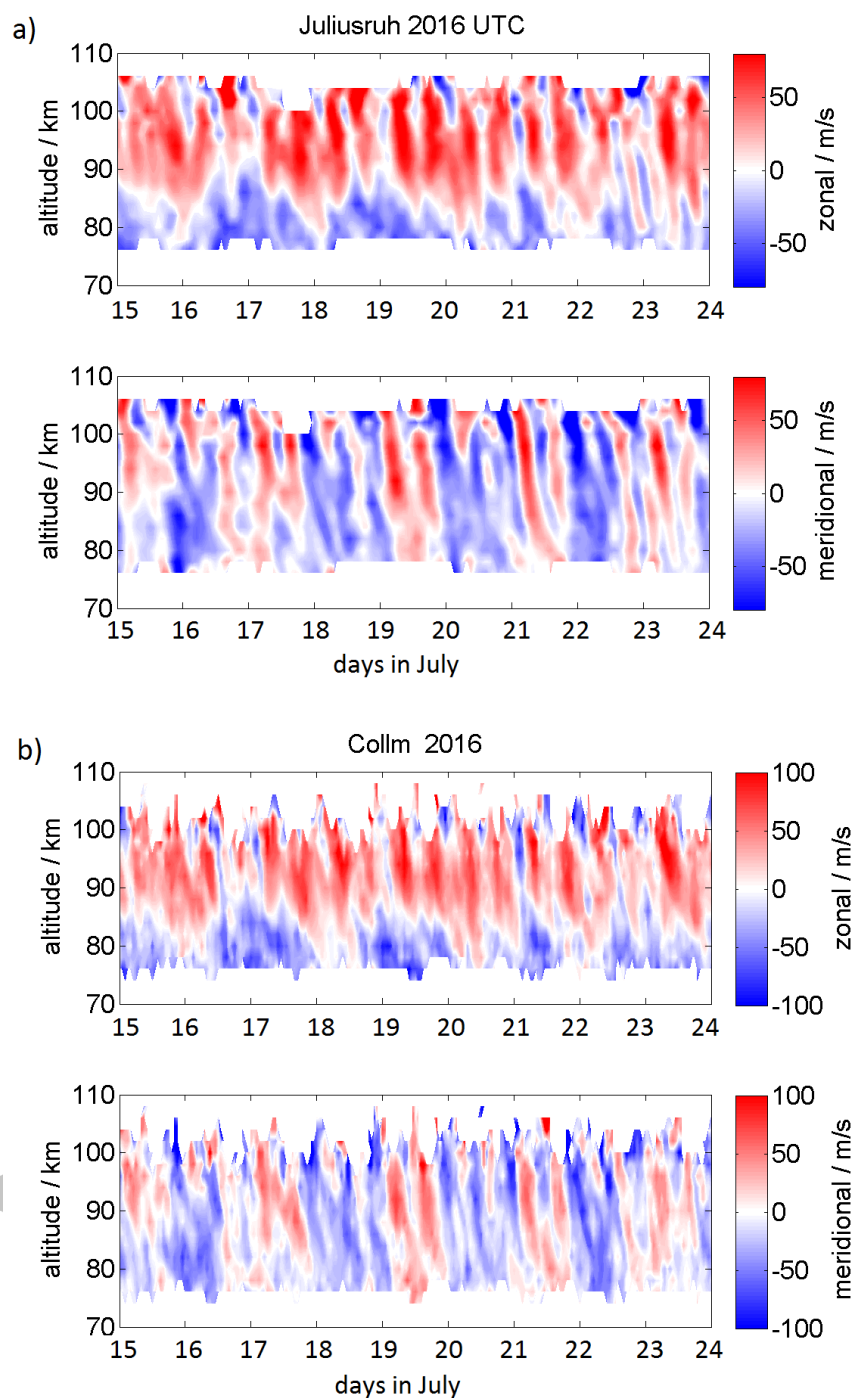


**Figure 8.** Meteor radar winds from (a) Juliusruh and (b) Collm, Germany. The abscissa ticks refer to 0 UT on the given day.

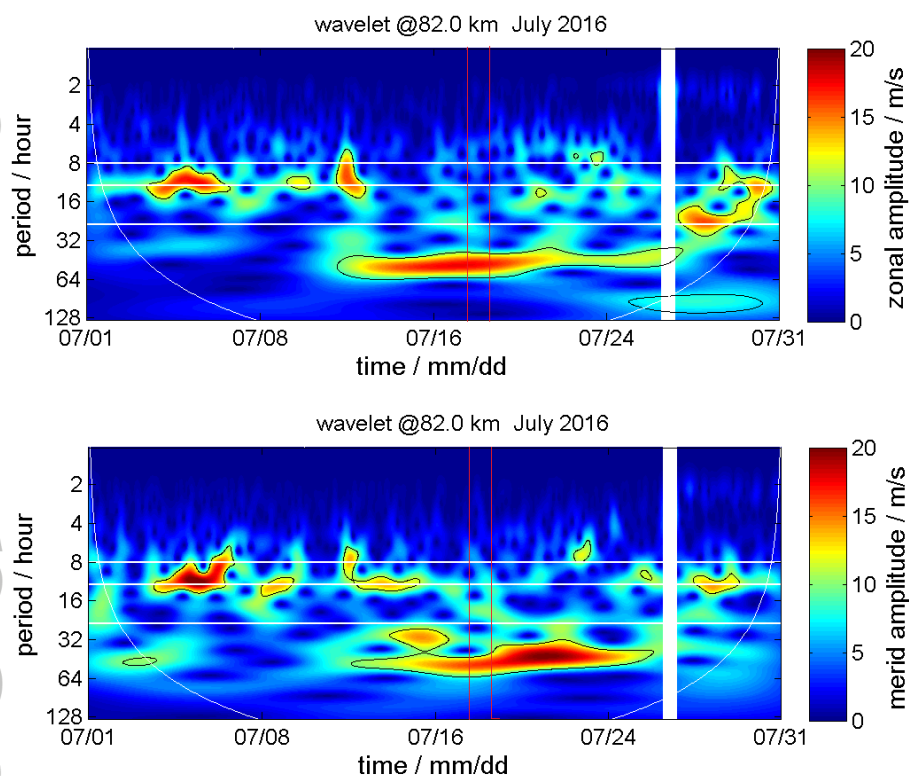


**Figure 9.** Quasi 2-day planetary wave visible in spectral analysis of (top) zonal and (bottom) meridional meteor radar winds above Juliusruh at 82 km altitude. The vertical red lines contain the time of NLC measurement. The corresponding spectra from Collm are very similar.

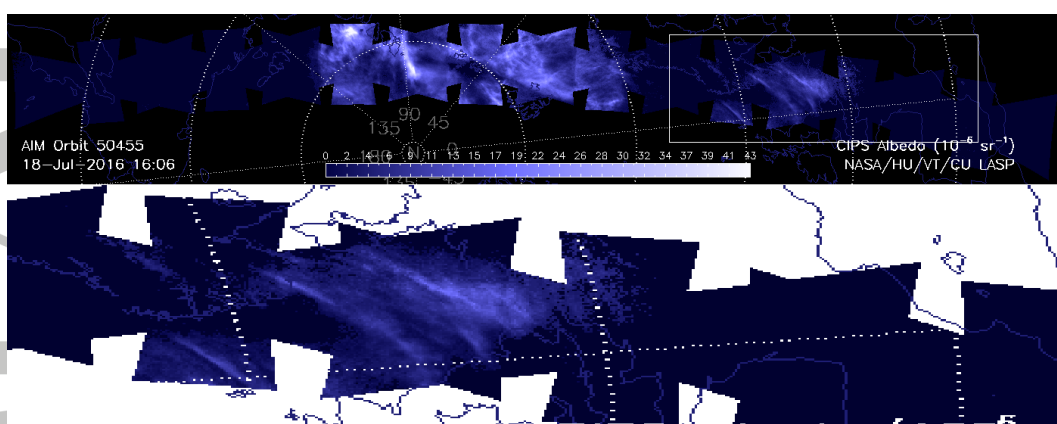


**Figure 10.** CIPS orbit strip 50455 (top) and close-up (bottom) at 16:06 UT on 18 July 2016 showing NLC above the North Sea ( $\approx 55^\circ\text{N}$ ,  $4^\circ\text{E}$ ) between Scotland and Denmark. Spain is located to the lower right.

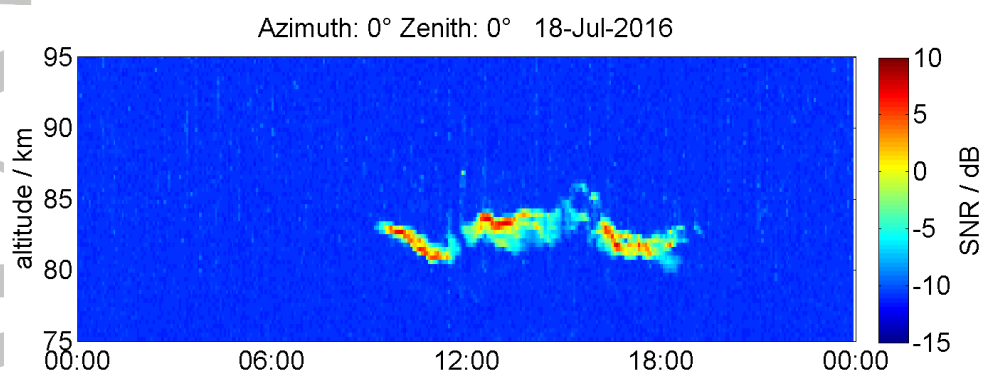


**Figure 11.** MSE above Kühlungsborn, recorded by the OSWIN radar on 18 July 2016.

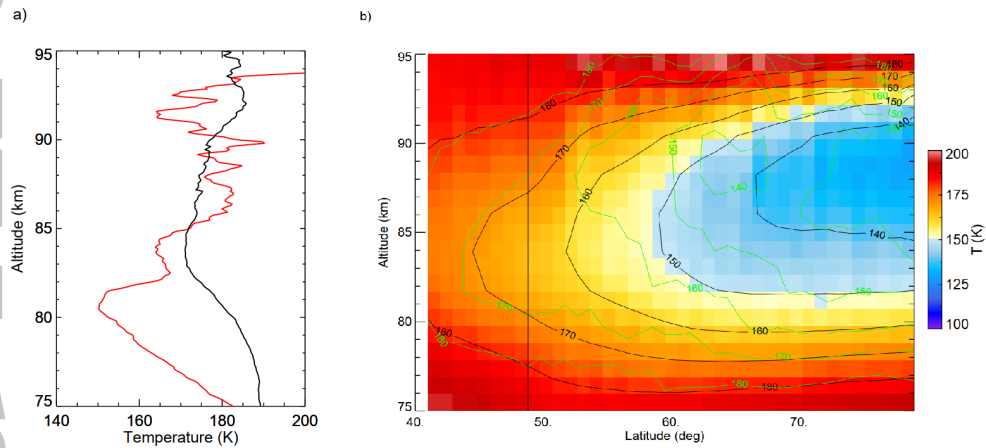


**Figure 12.** (a) Mean temperature profile in July measured by lidar (black line) and the temperature profile measured during the night of NLC observation (red line). (b) Latitudinal cross-section of the thermal state of the atmosphere in July for 0–30°E derived from SABER for the years 2002–2017. The contours of July 2016 are overdrawn in green.